Middle to late Miocene stepwise climate cooling: Evidence from a high-resolution deep water isotope curve spanning 8 million years

Ann Holbourn, Wolfgang Kuhnt, Steven Clemens, Warren Prell, and Nils Andersen Received 18 July 2013; revised 28 October 2013; accepted 4 November 2013; published 3 December 2013.

[1] We present high-resolution (2–3 kyr) benthic foraminiferal stable isotopes in a continuous, well-preserved sedimentary archive from the West Pacific Ocean (Ocean Drilling Program Site 1146), which track climate evolution in unprecedented resolution over the period 12.9 to 8.4 Ma. We developed an astronomically tuned chronology over this interval and integrated our new records with published isotope data from the same location to reconstruct long-term climate and ocean circulation development between 16.4 and 8.4 Ma. This extended perspective reveals that the long eccentricity (400 kyr) cycle is prominently encoded in the δ^{13} C signal over most of the record, reflecting long-term fluctuations in the carbon cycle. The δ^{18} O signal closely follows variations in short eccentricity (100 kyr) and obliquity (41 kyr). In particular, the obliquity cycle is prominent from ~14.6 to 14.1 Ma and from ~9.8 to 9.2 Ma, when high-amplitude variability in obliquity is congruent with low-amplitude variability in short eccentricity. The δ^{18} O curve is additionally characterized by a series of incremental steps at ~14.6, 13.9, 13.1, 10.6, 9.9, and 9.0 Ma, which we attribute to progressive deep water cooling and/or glaciation episodes following the end of the Miocene climatic optimum. On the basis of δ^{18} O amplitudes, we find that climate variability decreased substantially after ~13 Ma, except for a remarkable warming episode at ~10.8–10.7 Ma at peak insolation during eccentricity maxima (100 and 400 kyr). This transient warming, associated with a massive negative carbon isotope shift, is reminiscent of intense global warming events at eccentricity maxima during the Miocene climatic optimum.

Citation: Holbourn, A., W. Kuhnt, S. Clemens, W. Prell, and N. Andersen (2013), Middle to late Miocene stepwise climate cooling: Evidence from a high-resolution deep water isotope curve spanning 8 million years, *Paleoceanography*, 28, 688–699, doi:10.1002/2013PA002538.

1. Introduction

[2] During the Neogene, Earth's climate transitioned from a prolonged phase of global warmth (Miocene climatic optimum) into a colder mode with permanent polar ice, culminating with development of extensive Pleistocene ice sheets over the Northern and Southern Hemispheres [Zachos et al., 2001a, 2008]. The sequence of climate events and the processes which drove this profound climate transition are still poorly understood, because continuous, well-dated Miocene sedimentary archives are still extremely scarce. The prolonged middle to late Miocene interval of relative global warmth additionally offers an especially useful analogue to explore

the range of natural climate variability and to elucidate the main drivers of climate evolution during warmer climate modes. In particular, a better understanding of the dynamic behavior of the large East Antarctic ice sheet and of the processes and feedbacks driving long- and short-term climate variability in a warmer world is essential to better constrain projections of future climate development.

[3] In the last decades, high-resolution, astronomically tuned benthic stable isotopes have provided a powerful stratigraphical tool for the correlation of Cenozoic marine sequences and for documentation of secular variations in ice volume and ocean circulation [e.g., Zachos et al., 2001a, 2008; Lisiecki and Raymo, 2005; Pälike et al., 2006]. However, it has proven difficult to acquire continous, high-resolution data series over some extended intervals of the Miocene, in particular over the period known as the "Carbonate Crash" at ~9-11 Ma [Lyle et al., 2008], because deep marine sequences are frequently plagued by carbonate dissolution and poor recovery. The most recent deep-sea composite isotope compilations [e.g., Zachos et al., 2008; Cramer et al., 2009] indicate a long-term cooling trend from the middle to the late Miocene. Superimposed on this long-term trend, discrete cooling steps have been identified, in particular the Mi-Events [Miller et al., 1991], which correspond to positive oxygen isotope shifts marking episodes

¹Institute of Geosciences, Christian-Albrechts-University, Kiel Germany.

²Department of Geological Sciences, Brown University, Providence, Rhode Island, USA.

³Leibniz Laboratory for Radiometric Dating and Stable Isotope Research, Christian-Albrechts-University, Kiel, Germany.

Corresponding author: A. Holbourn, Institute of Geosciences, Christian-Albrechts-University, D-24118 Kiel, Germany. (ah@gpi.uni-kiel.de)

^{©2013.} American Geophysical Union. All Rights Reserved. 0883-8305/13/10.1002/2013PA002538

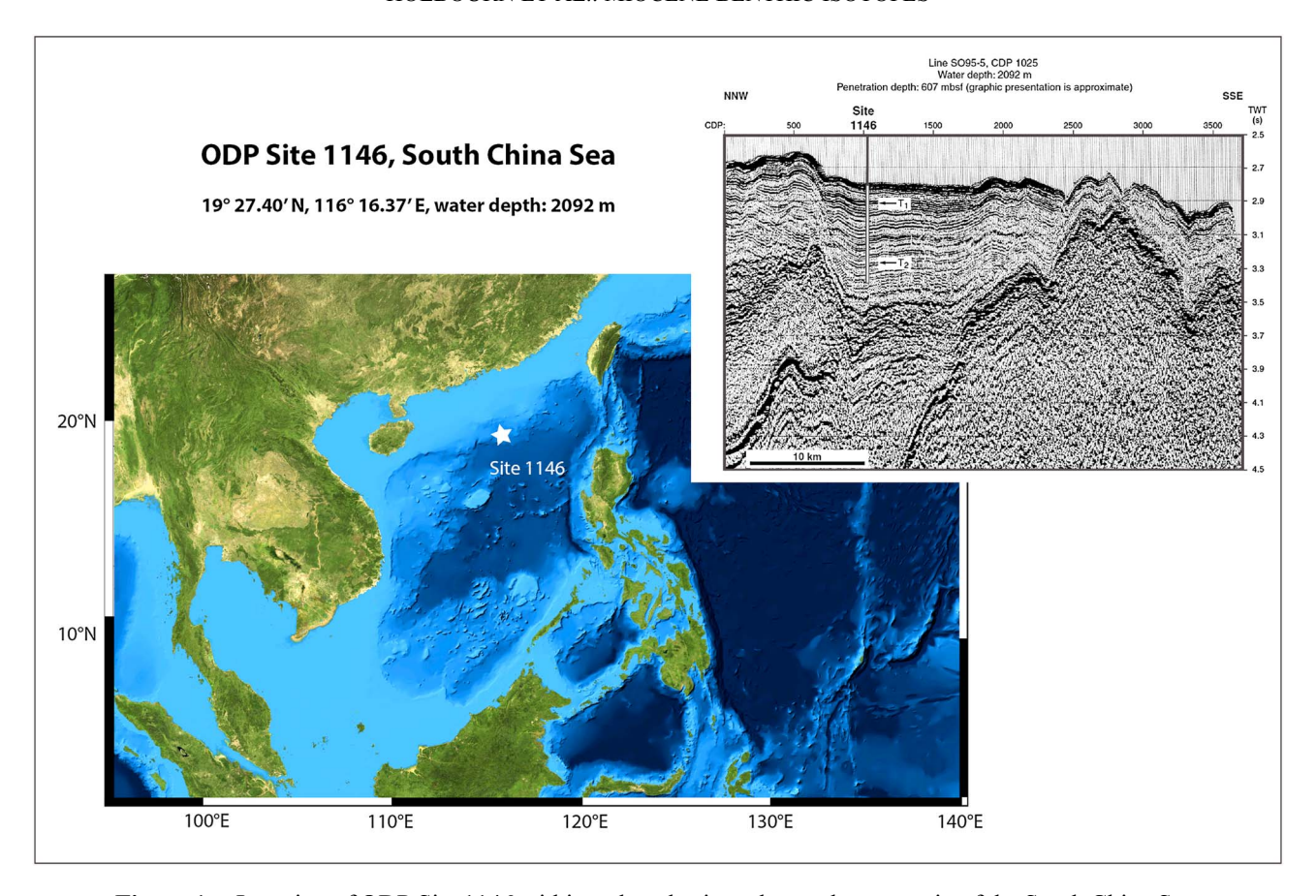


Figure 1. Location of ODP Site 1146 within a slope basin at the northern margin of the South China Sea. Satellite image and bathymetry from *Stöckli et al.* [2005], SO95-5 multichannel seismic line from *Wang et al.* [2000].

of intensified glaciation and/or deep water cooling, which offer potential for global correlations of marine sequences [Westerhold et al., 2005; John et al., 2001]. However, the definition and placement of these events have remained somewhat elusive, because most marine isotope records spanning this interval are of relatively low temporal resolution and do not capture the full spectrum of climate variability.

[4] Ocean Drilling Program (ODP) Site 1146 (19°27.40′N, 116°16.37′E, water depth: 2092 m, Figure 1) recovered in the South China Sea a continuous, clay-rich sedimentary succession spanning the middle to late Miocene [Wang et al., 2000]. A free connection existed between the South China Sea and the Pacific Ocean over most of this time interval, as the modern Bashi Strait (sill depth ~2600 m), which separates the South China Sea from the Pacific Ocean, only formed at ~6.5 Ma between Luzon and Taiwan as a result of the Luzon Arc collision [Huang et al., 1997; Wang et al., 2000]. During the Miocene, Site 1146 was at approximately the same latitude and water depth as today [Wang et al., 2000] and remained fully open to the western Pacific Ocean. Thus, the deep water signal in this site is fully representative of Pacific deep water masses originating in higher latitudes. Furthermore, the clay and carbonate-rich sequence in this site exhibits relatively high and constant sedimentation rates (2–3 cm/kyr) as well as excellent preservation of calcareous microfossils, thus providing an exceptional archive for reconstructing climate variations and Pacific circulation development over the Miocene.

[5] We present high-resolution (2–3 kyr time resolution), astronomically tuned benthic foraminiferal oxygen (δ^{18} O) and carbon (δ^{13} C) isotope data that closely track high-latitude climate change and deep water ventilation over the interval 12.9–8.4 Ma. We additionally provide a long-term perspective of Miocene climate variability by integrating these new data with previously published, high-resolution benthic isotope records from the same location, which focus on the interval 16.4–12.9 Ma [Holbourn et al., 2005, 2007]. This extended middle to late Miocene benthic isotope data set provides a high-resolution, astronomically tuned reference curve spanning 8 million years of Earth's climate history (16.4–8.4 Ma).

2. Material and Methods

2.1. Sampling Strategy

[6] Our study is based on Miocene marine sediments recovered at ODP Site 1146 (19°27.40′N, 116°16.37′E; water depth: 2092 m) in the South China Sea (Figure 1). Detailed site location, core recovery, and lithological descriptions can be found in *Wang et al.* [2000]. Cores were sampled in ~5 cm intervals (~2–3 kyr time resolution) from a composite sequence (shipboard splice) from Holes 1146A and 1146C (396.23–498.61 m composite depth). After comparison of the shipboard natural gamma ray, color reflectance, magnetic susceptibility data, and overlapping benthic

Table 1. Revised Splice Tie Points, ODP Site 1146^a

Hole, Core, Section, Interval (cm)	Depth mbsf	Depth mcd	Depth mcd revised		Hole, Core, Section, Interval (cm)	Depth mbsf	Depth mcd	Depth mcd Revised
1146A-36X-6, 132	337.22	359.32	359.32	Tie to	1146C-36X-3, 7	337.67	359.32	359.32
1146C-36X-6, 27	342.37	364.02	364.02	Tie to	1146A-37X-3, 17	341.27	364.02	364.02
1146A-37X-6, 77	346.37	369.12	369.12	Tie to	1146C-37X-2, 29.5	346.02	369.12	369.12
1146C-37X-6, 42	352.12	375.22	375.22	Tie to	1146A-38X-3, 74.5	351.47	375.22	375.22
1146A-38X-5, 82	354.52	378.27	378.27	Tie to	1146C-38X-1, 32	354.12	378.27	378.27
1146C-38X-4, 122	359.52	383.67	383.67	Tie to	1146A-39X-2, 107	359.87	383.67	383.67
1146A-39X-6, 27	365.07	388.87	388.87	Tie to	1146C-39X-1, 7	363.57	388.87	388.87
1146C-39X-5, 142	370.92	396.22	396.22	Tie to	1146A-40X-3, 152	371.42	396.22	396.22
1146A-40X-5, 132	374.22	399.02	399.02	Tie to	1146C-40X-1, 25.5	373.36	399.02	399.02
1146C-40X-4, 51	378.11	403.77	403.77	Tie to	1146A-41X-1, 143	377.93		403.77
1146A-41X-6, 23	384.23		410.07	Tie to	1146C-41X-1, 41	383.21		410.07
1146C-41X-3, 71	386.51		413.37	Tie to	1146A-42X-1, 103	387.13		413.37
1146A-42X-6, 97	394.57	418.89	420.81	Tie to	1146C-42X-2, 142	395.32	418.89	420.81
1146C-42X-5, 127	399.67	423.24	425.16	Tie to	1146A-43X-3, 4.5	398.77	423.24	425.16
1146A-43X-cc, 60	405.30		431.69	Append to	1146A-44X-1, 0	405.30		431.69
1146A-44X-5, 102	412.32	436.39	438.71	Tie to	1146C-44X-1, 147	413.07	436.39	438.71
1146C-44X-5, 132	418.92	442.24	444.56	Tie to	1146A-45X-2, 142	417.82	442.24	444.56
1146A-45X-5, 47	421.37	445.79	448.11	Tie to	1146C-45X-1, 87	422.07	445.79	448.11
1146C-45X-6, 17	428.87	452.59	454.91	Tie to	1146A-46X-2, 67	426.67	452.59	454.91
1146A-46X-5, 62	431.12	457.04	459.36	Tie to	1146C-46X-1, 12	430.72	457.04	459.36
1146C-46X-5, 42	437.02	463.34	465.66	Tie to	1146A-47X-1, 132	435.42	463.34	465.66
1146A-47X-6, 22	441.82	469.74	472.06	Tie to	1146C-47X-2, 64.5	442.37	469.74	472.06
1146C-47X-5, 107	447.27	474.64	476.96	Tie to	1146A-48X-2, 121	446.43	474.64	476.96
1146A-48X-6, 122	452.42	480.63	482.95	Tie to	1146C-48X-3, 22.5	453.04	480.63	482.95
1146C-48X-6, 17	457.47	485.06	487.38	Tie to	1146A-49X-3, 152	457.92	485.06	487.38
1146A-49X-6, 102	461.92	489.06	491.38	Tie to	1146C-49X-2, 104.5	462.07	489.06	491.38

^ambsf, metres below seafloor; mcd, meters composite depth.

isotope records over the splice tie points, we made the following modifications to the original shipboard splice:

- [7] 1. We compensated for a small gap at the junction of Section 1146C-40X-4 to Section 1146A-41X-1 by defining two new tie points in these sections, based on the match of isotope data from Holes 1146A and C. This adjustment resulted in the addition of 22 cm to the meters composite depth (mcd) scale.
- [8] 2. We corrected the original appendment of Section 1146A-41X-6 to Section 1146A-42X-1 and included sediment recovered below 86 cm in Section 1146A-41X-6 and in Sections 1146A-41X-7 and CC (~135 cm of sediment). We defined two new tie points and inserted a new splice segment from Hole 1146C, based on the match of isotope data from Holes 1146A and C. This adjustment resulted in the addition of 170 cm to the mcd scale.
- [9] 3. We corrected the original appendment of Section 1146A-43X-6 to Section 1146A-44X-1 and included sediment recovered in Section 1146A-43X-CC (~33 cm of sediment). Taking into account the potential loss of sediment at the end of the core barrel, this adjustment resulted in the addition of 40 cm to the mcd scale.
- [10] These modifications to the original shipboard splice resulted in the addition of 232 cm to the mcd depth scale. The revised splice tie points are shown in Table 1.

2.2. Isotope Analysis

[11] All samples were oven dried at 40° C and weighed before washing over a $63 \mu m$ sieve. Residues were oven dried at 40° C on a sheet of filter paper, then weighed and sieved into different size fractions. We measured δ^{18} O and δ^{13} C in the epifaunal benthic foraminifers *Planulina wuellerstorfi* and/or *Cibicidoides mundulus*. Well-preserved tests were broken into large fragments, cleaned in alcohol in an ultrasonic bath, and then dried

at 40°C. Measurements were made with the Finnigan MAT 251 mass spectrometer at the Leibniz Laboratory, Kiel University. The instrument is coupled online to a Carbo-Kiel Device (Type I). Samples were reacted by individual acid addition (99% H₃PO₄ at 73°C). Standard external error is better than $\pm 0.07\%$ and $\pm 0.05\%$ for δ^{18} O and δ^{13} C, respectively. Replicate measurements on ~4% of samples indicate mean reproducibility better than $\pm 0.09\%$ for $\delta^{18}O$ and $\delta^{13}C$, respectively. Paired measurements in middle Miocene samples from Ocean Drilling Program (ODP) Sites 1146 and 1237 previously indicated no significant offset in $\delta^{18}O$ and $\delta^{13}C$ between P. wuellerstorfi and C. mundulus [Holbourn et al., 2007]. Results were calibrated using the National Institute of Standards and Technology (Gaithersburg, Maryland) carbonate isotope standard NBS 20 and NBS 19 and 18, and are reported on the Vienna PeeDee belemnite (V-PDB) scale. Data sets are archived at the World Data Center for Marine Environmental Sciences (WDC-MARE) (http://www.pangaea.de).

2.3. Chronology

[12] The revised shipboard planktonic foraminiferal and nannofossil biostratigraphy in *Nathan and Leckie* [2003] with updated ages from *Gradstein et al.* [2012] and *Wade et al.* [2011] provided the framework to develop an astronomically tuned age model over the interval 12.9–8.4 Ma in Site 1146. We generated a new chronology over the 12.9–8.4 Ma interval in Site 1146 by correlating the benthic foraminiferal δ^{18} O series to computed variations of the Earth's orbit (obliquity and eccentricity in *Laskar et al.*, 2004), essentially following the strategy outlined in *Holbourn et al.* [2005, 2007] for the tuning of the 16.4–12.9 Ma interval in Site 1146. As tuning target, we constructed an eccentricity-tilt composite (ET) with no phase shift and with equal weight of eccentricity

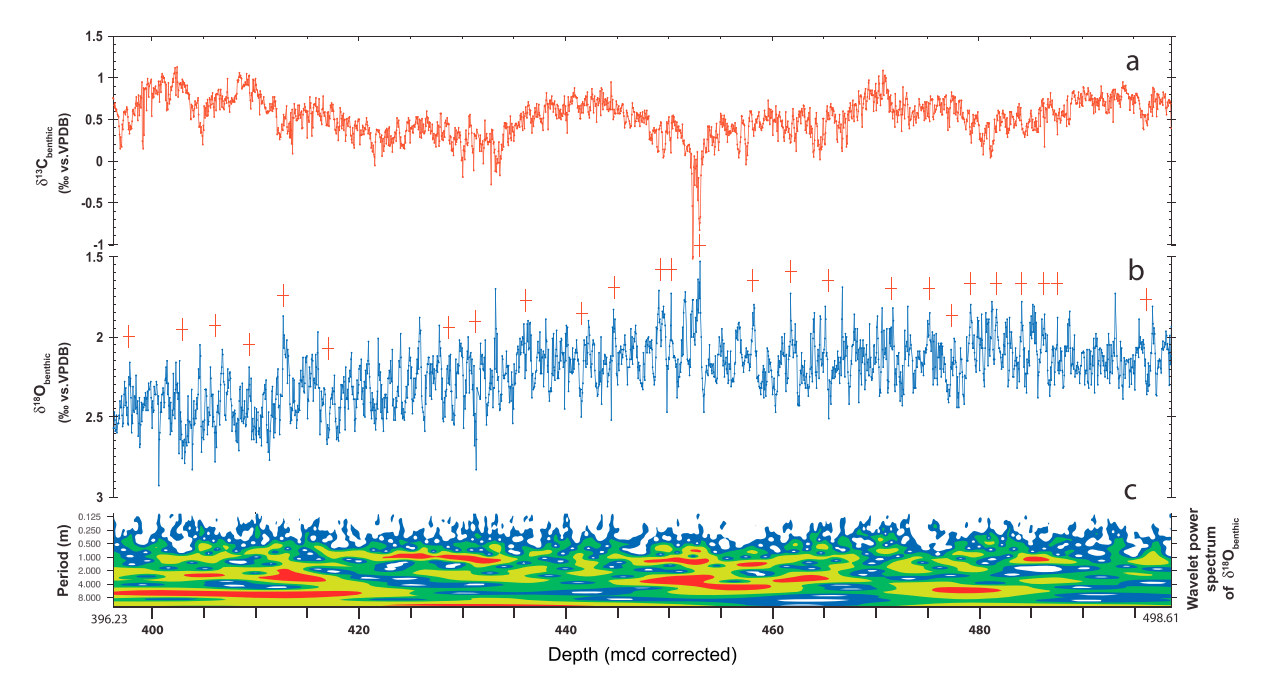


Figure 2. Benthic δ^{18} O and δ^{13} C versus depth (corrected mcd) in ODP Site 1146; (a) benthic δ^{13} C; (b) benthic δ^{18} O, tie points to La2004 [*Laskar et al.*, 2004] are indicated by red crosses; (c) wavelet power spectrum of benthic δ^{18} O using a Morlet wavelet with six parameters, scale width of 0.01, and start scale of 2, contour levels represent more than 75% (red), 50% (yellow), 25% (green), and 5% (blue) of wavelet power.

and obliquity. We applied a minimal tuning strategy in order to preserve original spectral characteristics, already evident in the depth domain, and to avoid artificial changes in sedimentation rates [Muller and MacDonald, 2000]. The δ^{18} O and δ^{13} C profiles from Site 1146 are plotted versus depth in Figure 2. Orbital tuning and calculation of sedimentation rates were performed with AnalySeries 2.0.4.2 [Paillard et al., 1996]. Wavelet software for time series analysis was provided by C. Torrence and G. Compo and is available at URL: http://atoc.colorado.edu/research/wavelets/. Details of wavelet analysis are available in Torrence and Compo [1998].

2.4. Ice Volume Model

[13] We used the ice volume model of *Imbrie and Imbrie* [1980] forced by 75°S insolation to investigate whether the 1146 δ^{18} O curve showed similarity to modeled ice volume during a remarkable warming episode at ~10.8–10.7 Ma. The model setup corresponds to a system function of the optimum model for Pleistocene Northern Hemisphere ice sheets. It prescribes a system time constant of 17 kyr (time lag of maximum insolation to minimum ice volume) and a ratio of 4:1 between the time constants of glacial growth and melting (melting four times faster than ice buildup).

3. Results

3.1. Astronomically Tuned Chronology

[14] The 1146 stable isotope data over the 12.9–8.4 Ma interval are plotted against composite depth in Figure 2 and against age in Figures 3 and 4. Age tie points between $\delta^{18}O$ and ET series are shown in Figures 2 and 4 and Table 2. The average sedimentation rate is ~ 2.3 cm kyr⁻¹ with a maximum of 3.0 cm kyr⁻¹ and a minimum sedimentation rate of

 1.7 cm kyr^{-1} (Figure 4). This corresponds to a chronological resolution of $\sim 2-3$ kyr for the stable isotope time series.

[15] The benthic δ^{18} O and δ^{13} C series exhibit high- and low-frequency fluctuations that correspond to cyclic changes in obliquity and eccentricity over the 12.9–8.4 Ma interval. Comparison of δ^{18} O and δ^{13} C plotted in the depth and time domains reveals that original spectral characteristics are preserved following the tuning procedure (Figures 2–4). We note that the short eccentricity (100 kyr) and obliquity (41 kyr) periods are prominent in the untuned δ^{18} O record (Figure 2). In particular, the low amplitude of short eccentricity between ~9.8 and 9.2 Ma is clearly reflected in the δ^{18} O series, which predominantly exhibits 41 kyr variability over this interval. Superimposed on higher frequency variations, the untuned δ^{13} C series displays prominent low-frequency oscillations that broadly relate to the ~400 kyr long eccentricity cycle, particularly over the interval $\sim 11-8.4$ Ma.

3.2. Temporal Evolution of δ^{18} O and δ^{13} C (12.9–8.4 Ma)

[16] Mean δ^{13} C values generally fluctuate between 0 and 1‰, except for two abrupt negative shifts reaching \sim -0.8 and \sim -1.2‰ at 10.78 and 10.75 Ma (Figures 3 and 4). Amplitude variability is generally between 0.2 and 0.8‰, except during the negative shifts, where it reaches >1.6‰. The δ^{18} O curve reveals a long-term glacial expansion and deep water cooling with most of the δ^{18} O increase occurring in three distinct steps after 10.6, 9.9, and 9.0 Ma. Based on the δ^{18} O signal, we identify two distinct phases of climate evolution through the interval 12.9 to 8.4 Ma.

[17] During Phase 1 (12.9 to 9.9 Ma), δ^{18} O shows a response to both obliquity and (100 kyr) eccentricity forcing

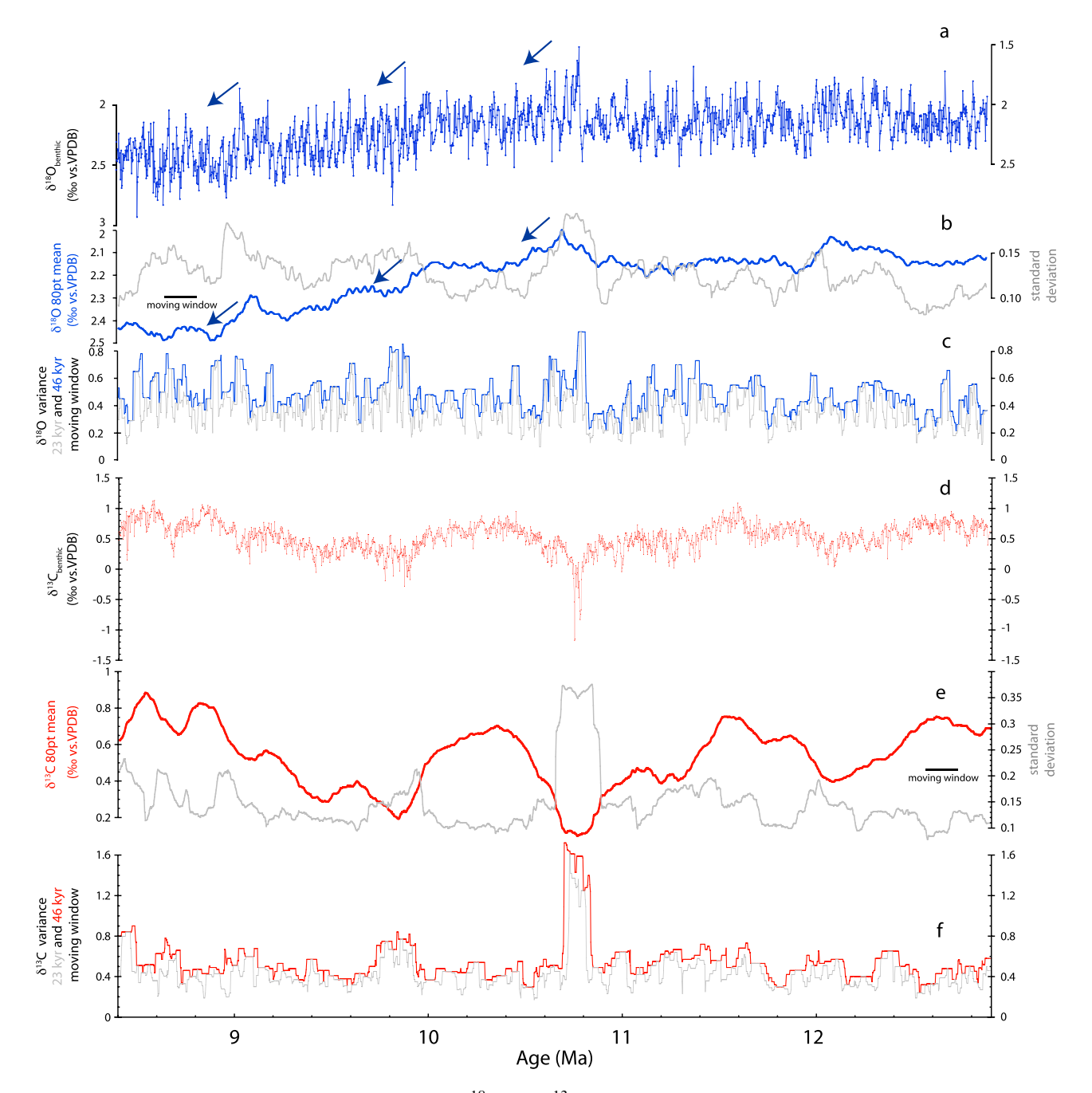


Figure 3. Temporal evolution of benthic $\delta^{18}O$ and $\delta^{13}C$ in ODP Site 1146 over 12.9–8.4 Ma interval; (a) benthic $\delta^{18}O$, blue arrows mark glacial expansion and/or deep water cooling after 10.6, 9.9, and 9.0 Ma; (b) running mean and standard deviation of $\delta^{18}O$ (80 point (pt) corresponding to ~180 kyr moving window), blue arrows as in Figure 3a; (c) amplitude variance in $\delta^{18}O$ (23 and 46 kyr moving windows); (d) benthic $\delta^{13}C$; (e) running mean and standard deviation of $\delta^{13}C$ (80 point (pt) corresponding to ~180 kyr moving window); (f) amplitude variance in $\delta^{13}C$ (23 and 46 kyr moving windows).

(Figures 3 and 4). Mean δ^{18} O values oscillate between 2.0 and 2.2‰ with amplitude varying between 0.2 and 0.6‰, except at ~10.8–10.7 Ma, when mean values decrease to 2.0‰ and amplitude variability increases to 0.7–0.9‰. Salient features during Phase 1 are the dampened variability at 12.7–12.5 and 11.0–10.8 Ma, pointing to prolonged episodes of remarkably stable ice volume, and the transient warming spikes that coincide with intense δ^{13} C minima at ~10.8–10.7 Ma, following peak southern hemisphere

insolation (Figures 4 and 5). Following this warming episode, mean values increase to 2.2% and amplitude variability is sustained at ~0.4% until 9.9 Ma (Figure 3).

[18] During Phase 2 (9.9–8.4 Ma), mean δ^{18} O values are sustained at ~2.3–2.4% and ~2.4–2.5%, following increases after 9.9 and 9.0 Ma, respectively (Figures 3 and 4). Amplitude variations between 0.4 and 0.8% are slightly higher than during Phase 1. The cooling step at ~9.9 Ma initiated a new mode of climate variability with enhanced

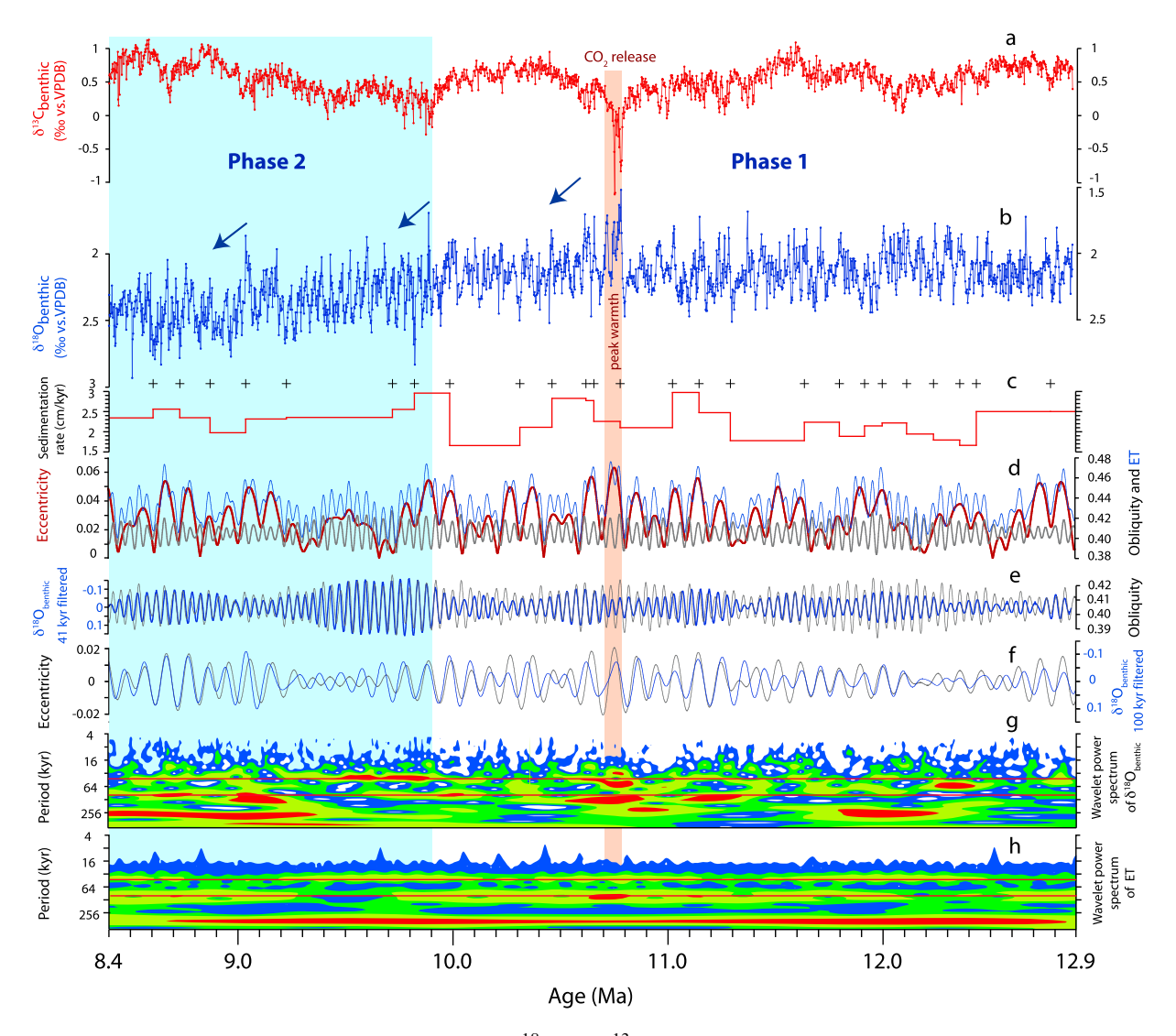


Figure 4. High-resolution (2–3 kyr) benthic $\delta^{18}O$ and $\delta^{13}C$ in ODP Site 1146 over 12.9–8.4 Ma interval. (a) benthic $\delta^{13}C$; (b) benthic $\delta^{18}O$, blue arrows mark glacial expansion and/or deep water cooling after 10.6, 9.9, and 9.0 Ma; (c) sedimentation rates, tie points to La2004 [*Laskar et al.*, 2004] are indicated by gray crosses; (d) eccentricity, obliquity, and eccentricity plus obliquity (ET) from *Laskar et al.* [2004]; (e) 41 kyr filtered benthic $\delta^{18}O$ using Gaussian filter with bandwidth of 0.004 centered at frequency of 0.0243 and obliquity; (f) 100 kyr filtered benthic $\delta^{18}O$ and eccentricity using Gaussian filter with bandwidth of 0.003 centered at frequency of 0.01; (g) wavelet power spectrum of benthic $\delta^{18}O$ using Morlet wavelet with six parameters, scale width of 0.01, and start scale of 2, contour levels represent more than 75% (red), 50% (yellow), 25% (green), and 5% (blue) of wavelet power; (h) wavelet power spectrum of ET (settings are the same as in Figure 4f). Orange band marks transient warming and negative $\delta^{13}C$ excursion between 10.8 and 10.7 Ma. Climate phase 1 (12.9–9.9 Ma) unshaded, climate phase 2 (9.9–8.4 Ma) shaded light blue.

sensitivity to obliquity forcing between 9.8 and 9.2 Ma during a protracted interval of low (100 kyr) eccentricity and high obliquity variability. Glacial-interglacial $\delta^{18}{\rm O}$ cycles additionally exhibit a more pronounced asymmetry during this interval, indicating a change in internal climate dynamics driving rapid deglaciations and slower glaciations. A change back to high-amplitude (100 kyr) eccentricity after 9.2 Ma coincided with two warming intervals with substantially lighter $\delta^{18}{\rm O}$ between 9.2 and 9.0 Ma, followed by renewed cooling after 9.0 Ma during a period of low obliquity variability. In this latter colder mode, glacial-interglacial

cycles continue to show high-amplitude variability with pronounced 41 and 100 kyr rhythms.

4. Discussion

4.1. Ice Volume Contribution to $\delta^{18}O$ Variability (12.9–8.4 Ma)

[19] The relative contribution of ice volume and temperature to the benthic $\delta^{18}O$ signal fluctuated considerably over the last 35 Myr, mainly due to changes in the size and stability of Southern and Northern Hemisphere ice sheets and to

Table 2. Age Control Points Used to Derive Astronomically Tuned Timescale (12.9 – 8.4 Ma) in ODP Site 1146

Depth	Age		
(mcd corrected)	(ka)		
397.75	8,384		
402.88	8,602		
406.07	8,727		
409.37	8,868		
412.66	9,034		
417.04	9,223		
428.67	9,717		
431.28	9,819		
436.15	9,984		
441.58	10,312		
444.73	10,461		
449.19	10,619		
450.23	10,656		
453.00	10,779		
458.11	11,022		
461.80	11,146		
465.42	11,293		
471.55	11,637		
475.19	11,800		
477.40	11,917		
479.17	12,000		
481.68	12,113		
484.12	12,238		
486.31	12,360		
487.60	12,438		
496.23	12,783		

variations in the source and rate of deep water production [Billups and Schrag, 2002; De Boer et al., 2010]. Sedimentological evidence and modeling studies indicate that a large ice sheet has been present in East Antarctica since at least the middle Miocene [Lewis et al., 2007, 2008; DeConto et al., 2008; Haywood et al., 2009]. However, wetter and warmer conditions probably resulted in a δ^{18} O ice signal closer to that of modern Greenland or glacial Northern Hemisphere ice sheets (-35-40%) in contrast to -56.5%for the present-day East Antarctic Ice Sheet [Lhomme et al., 2005]). Thus, melting of ~15% of the East Antarctic Ice Sheet (EAIS), equivalent to a ~11 m sea level rise, would produce a decrease of 0.1% in benthic $\delta^{18}O$ during the middle to late Miocene, whereas today the same isotopic effect is achieved by melting only ~10% of the EAIS, equivalent to a ~7 m sea level rise [Huybrechts, 2000].

[20] Waxing and waning of ephemeral ice sheets on West Antarctica and Greenland cannot account for the amplitude of middle to late Miocene sea level and δ^{18} O variations (~0.5‰ in Site 1146, Figures 3 and 4; ~0.7‰ in Site 1085 [Westerhold et al., 2005]) over the 12.9–8.4 Ma interval. Today, complete melting of the West Antarctic Ice Sheet (WAIS) would result in a δ^{18} O seawater depletion of only 0.13% [Lhomme et al., 2005], translating to ~0.1% during the warmer Miocene period. This effect would be further decreased for a smaller Miocene WAIS. The contribution from a reduced Greenland ice sheet would also fall below the present-day isotopic contribution of 0.07‰ and be therefore almost negligible. Thus, a more realistic scenario is that a substantial part of the $\delta^{18}O$ variability between 12.9 and 8.4 Ma was due to a dynamic EAIS. A 50% ice volume contribution to deep water δ^{18} O is probably a conservative estimate, since Mg/Ca-based reconstructions suggest relatively

low $(1-2^{\circ}\text{C})$ deep water temperature fluctuations and comparatively high (0.5%) seawater $\delta^{18}\text{O}$ variability between 13 and 11.5 Ma [Lear et al., 2010]. Assuming that about half (0.2-0.3%) of the 1146 $\delta^{18}\text{O}$ variability (mean amplitude variability: 0.48% at the obliquity band) is due to ice volume fluctuations, this would be equivalent to melting of the whole WAIS and about 15–30% of the EAIS. These ice volume variations correspond to sea level fluctuations of ~20–30 m, in broad agreement with Miocene backstripped eustatic estimates [Kominz et al., 2008].

4.2. Transient Global Warming at ~10.8–10.7 Ma

[21] An intriguing feature in the 1146 δ^{18} O record is the abrupt warming event (δ^{18} O drop of ~1‰) at ~10.8 Ma associated with a massive decline of $\sim 1\%$ in δ^{13} C (Figures 4 and 5). Following a transient recovery, a second warming pulse at ~10.75 Ma coincides with a further, even more pronounced δ^{13} C decrease (~1.2%). These δ^{18} O and δ^{13} C minima represent prominent end-members within a background of orbitally paced δ^{18} O and δ^{13} C oscillations (100 and 41 kyr). The δ^{18} O shifts at ~10.8–10.7 Ma are reminiscent of prominent, transient warming events (~1% decreases), paced by 100 kyr eccentricity, within the warmer climatic optimum interval between ~16.4 and 14.6 Ma (Figures 6 and 7). These massive warming spikes, reported from the Pacific, Atlantic, and Southern Oceans [Woodruff and Savin, 1991; Flower and Kennett, 1993, 1995; Shackleton, 2001; Raffi et al., 2006; Holbourn et al., 2007], were also associated with abrupt negative δ^{13} C excursions. However, these middle Miocene high-amplitude δ^{18} O and δ^{13} C fluctuations (~1‰) occurred at a time when ice volume was substantially reduced [Lewis et al., 2006; Warny et al., 2009; Feakins et al., 2012; Hauptvogel and Passchier, 2012], implying that they cannot be solely attributed to ice volume changes but also reflect major changes in deep and intermediate water temperature and ventilation.

[22] In contrast, the late Miocene warming event at ~10.8– 10.7 Ma is rather exceptional, as it postdates the major glacial expansion at ~13.9 Ma, which suggests that melting of polar ice was involved during this extreme event. The striking similarity of the 1146 δ^{18} O curve to modeled ice volume between 10.8 and 10.6 Ma supports that δ^{18} O variations were driven by Antarctic ice dynamics in a manner that bears resemblance to Pleistocene climatic cycles forced by Northern Hemisphere insolation (Figure 5). The remarkable warming at ~10.8-10.7 Ma and the most extreme episode of warmth at ~15.6 Ma during the Miocene climatic optimum coincide with maxima in eccentricity (100 kyr, 400 kyr, and 2.4 Myr amplitude modulation) and in obliquity (1.2 kyr modulation), implicating insolation as a contributing trigger of these exceptional warming events. However, unlike the earlier ~15.6 Ma warming episode, the late Miocene warm event at ~10.8-10.7 Ma has not been identified in other records, possibly reflecting the scarcity of continuous, highresolution benthic isotope data spanning this interval.

[23] The magnitude of the δ^{13} C decreases associated with the δ^{18} O minima at ~10.8 Ma preclude that they are solely driven by local export flux and remineralization of particulate organic matter. Similar transient deep water warming and acidification episodes during warmer intervals of Earth's history such as the Eocene have been linked to rapid CH₄ or CO₂ release into the ocean/atmosphere system from

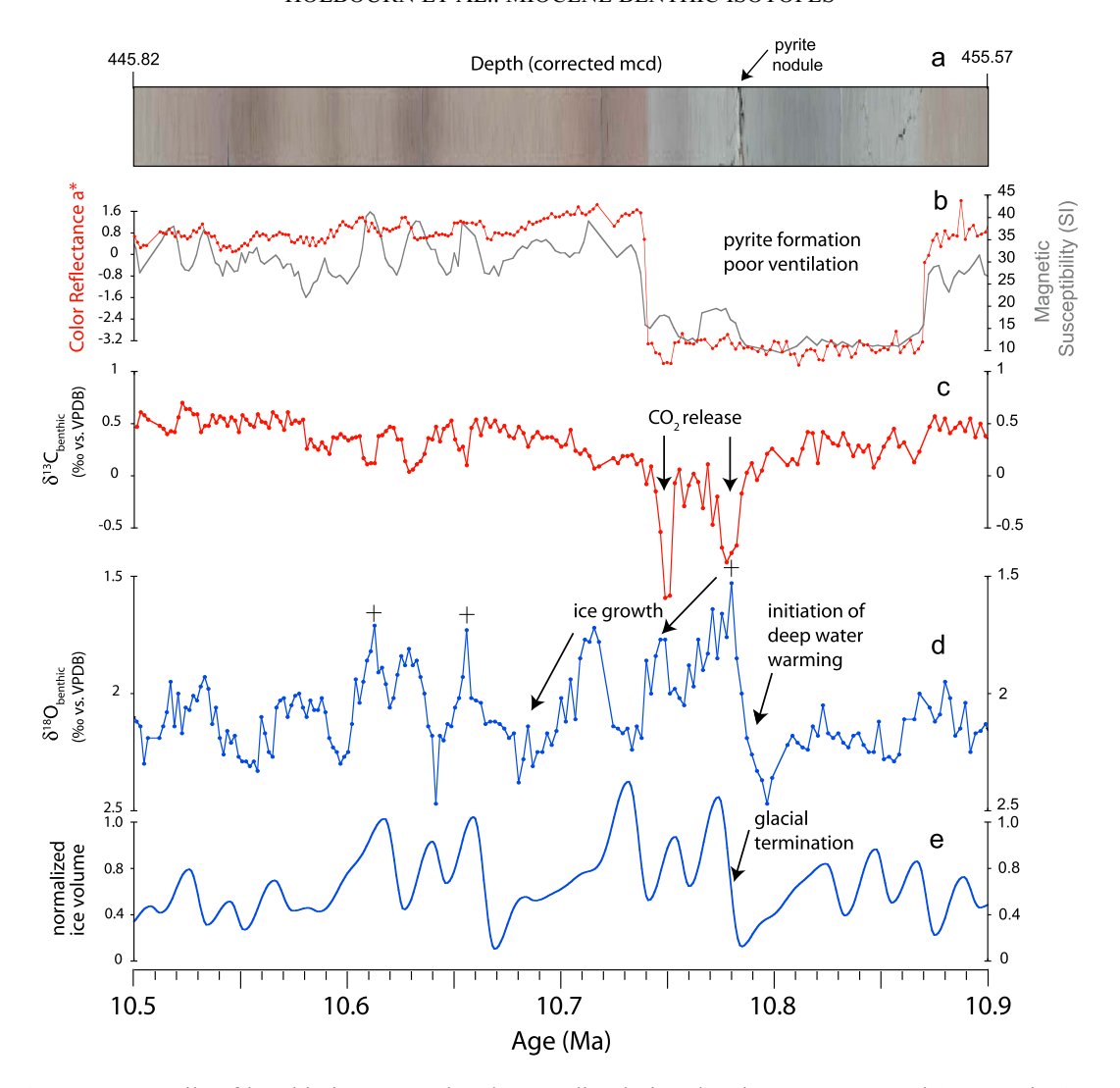


Figure 5. Details of benthic isotope and carbonate dissolution data between 10.9 and 10.5 Ma in ODP Site 1146; (a) digitized core photograph showing characteristic greenish gray sediment color with nodular pyrite across interval of poor deep water ventilation; (b) color reflectance a* and magnetic susceptibility; (c) benthic δ^{13} C; (d) benthic δ^{18} O shows striking similarity to modeled ice volume; note minimal tuning of - δ^{18} O to ET [*Laskar et al.*, 2004], tuning tie points indicated by gray crosses; (e) normalized predicted ice volume change (0 corresponding to fully glaciated Antarctica) from ice volume model forced by 75°S insolation.

various sources including methane-clathrate destabilization, magmatic degassing, and oxidation of dissolved organic carbon in the deep ocean [Dickens et al., 1995; Lourens et al., 2005; Zachos et al., 2008; Bohaty et al., 2009; Sexton et al., 2011]. In Site 1146, sedimentological evidence indicates that an extended period of reduced deep water ventilation with pyrite formation at the seafloor preceded the unusual transient warming events (Figure 5), supporting that the δ^{13} C spikes may be related to a prolonged episode of 13 C depletion in the deep ocean. However, it remains unclear to which extent this event had a regional impact or was associated with a more widespread reorganization in intermediate and deep water circulation. We speculate that increased deep water stratification after ~10.9 Ma may have promoted widespread storage of dissolved inorganic and organic carbon and acidification of deep water masses. This long-term trend appears to have been reversed after ~10.75 Ma, when the two

intense warming pulses led to "glacial termination-style" enhanced ocean mixing and CO₂ release to the atmosphere [Skinner et al., 2013], fuelling warming and ice decay at insolation maxima.

4.3. Middle to Late Miocene Stepwise Climate Cooling (16.4–8.4 Ma)

[24] Integrated benthic stable isotope data in Site 1146 spanning the interval 16.4–8.4 Ma track the Miocene transition from relatively warm climate conditions with reduced and highly variable ice cover over Antarctica to an increasingly glaciated mode with more permanent ice sheets (Figures 6 and 7). The δ^{18} O series shows that Antarctic glaciation progressed in a series of incremental steps at ~14.6, 13.9, 13.1, 10.6, 9.9, and 9.0 Ma, which are clearly expressed by sustained increases in mean δ^{18} O. The two most dramatic steps at ~13.9 and 13.1 Ma, which correspond to the Mi3- and Mi4-Events of

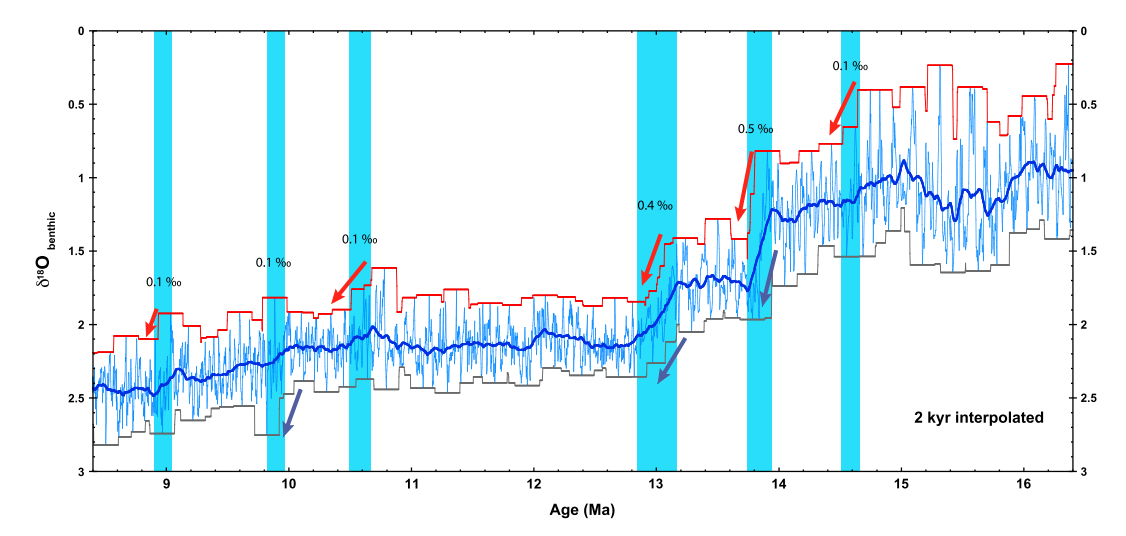


Figure 6. Integrated δ^{18} O record in ODP Site 1146 over 16.4–8.4 Ma interval (interpolated in 2 kyr steps, which is close to original data resolution) with 200 kyr window running mean, maximum (blue) and minimum (red). Arrows indicate mean δ^{18} O increases, resulting from increases in lighter (red arrows) and heavier values (blue arrows). Major changes in both heavy and light values at ~13.9 and 13.1 Ma probably include a considerable component of ice volume change. Blue shading highlights main cooling steps between 16.4 and 8.4 Ma.

Miller et al. [1991], exhibit substantial increases in both heavier and lighter values $\delta^{18}O$ (0.4–0.5‰) together with distinct decreases in amplitude variability. In contrast, the other four cooling steps are less pronounced, showing smaller increases (~0.1‰) in either lighter or heavier values.

[25] We speculate that the major δ^{18} O shifts at ~13.9 and 13.1 Ma reflect fundamental climate transitions and thresholds in glaciation, resulting in modified responses of the ocean/climate system to forcings. Prior to ~14.6 Ma, a smaller EAIS, mainly confined to the interior of the continent, probably grew and decayed rapidly in response to winter precipitation and summer radiative forcing patterns, in a manner comparable to Pleistocene Northern Hemisphere ice sheets. Following expansion at ~13.9 and 13.1 Ma, the EAIS became increasingly stable and less susceptible to melting due to a combination of factors including higher elevation, colder temperatures, increased thermal isolation of Antarctica, and decreased moisture flux from the lower latitudes. The smaller δ^{18} O increases at ~10.6, 9.9, and 9.0 Ma following the major glacial transitions at ~13.9 and 13.1 Ma indicate smaller-scale glacial expansions and/or further cooling of deep water masses originating from high latitudes.

Site 1085 [Westerhold et al., 2005] reveals a comparable long-term cooling trend between 14.0 and 8.8 Ma with several incremental steps and values exhibiting an overall increase from ~1 to ~2.5‰. The prominent steps at ~13.9 and 13.1 Ma corresponding to the Mi3- and Mi4-Events are clearly identified, supporting that these major increases are mainly related to high-latitude climate cooling and glacial expansion. However, the timing of subsequent cooling episodes differs to some extent in the δ^{18} O records from Sites 1085 and 1146. In particular, a sustained δ^{18} O increase between 11.5 and 10.4 Ma and a decreasing trend after 8.8 Ma are not apparent in the 1146 curve. The 1085 δ^{18} O record additionally exhibits higher variability, which may be due to the shallower water depth at this site. A possible

explanation is that these differences reflect regional changes in the composition of intermediate and deep water masses in the Atlantic and Pacific Oceans. The onset or intensification of North Atlantic deep water export is supported by benthic δ^{13} C compilations from multiple ocean sites [Poore et al., 2006; Cramer et al., 2009], indicating an intensification of interbasin gradients after ~12 or ~13 Ma, which has been ascribed to North Atlantic deep water formation. However, the timing of this event remains poorly constrained, and continuous, high-resolution records from the North Atlantic are needed to substantiate this view. Detailed comparison with high-resolution records from the Pacific and Indian Oceans would also be crucial to assess to what extent the δ^{18} O signals from these two sites are influenced by regional or global circulation trends and ice volume variations.

4.4. Climatic Response to Orbital Forcing

[27] The extended Site 1146 record allows us to evaluate the long-term relationship between astronomical forcing and the response of the ocean/climate, which is embedded in the benthic isotope data set (Figure 7). The long eccentricity (400 kyr) cycle is prominently encoded in the δ^{13} C record through most of the middle to late Miocene (16.4–8.4 Ma). The short eccentricity (100 kyr) and obliquity cycles (41 kyr) are clearly imprinted in both the δ^{18} O and δ^{13} C signals. However, enhanced 100 kyr variability stands out in the δ^{18} O and δ^{13} C series between ~16.4 and 14.6 Ma during the climatic optimum, whereas the signals become considerably dampened in two successive steps after ~14.6 Ma and after ~13 Ma. The obliquity cycle is especially prominent from ~14.6 to 14.1 Ma and from ~9.8 to 9.2 Ma during configurations of the Earth's orbit occurring only every ~2.4 Ma, when high-amplitude variability in obliquity is congruent with extremely low amplitude variability in short eccentricity. The long-term evolution of our isotope signals, thus, demonstrates that astronomical forcing has a major impact on

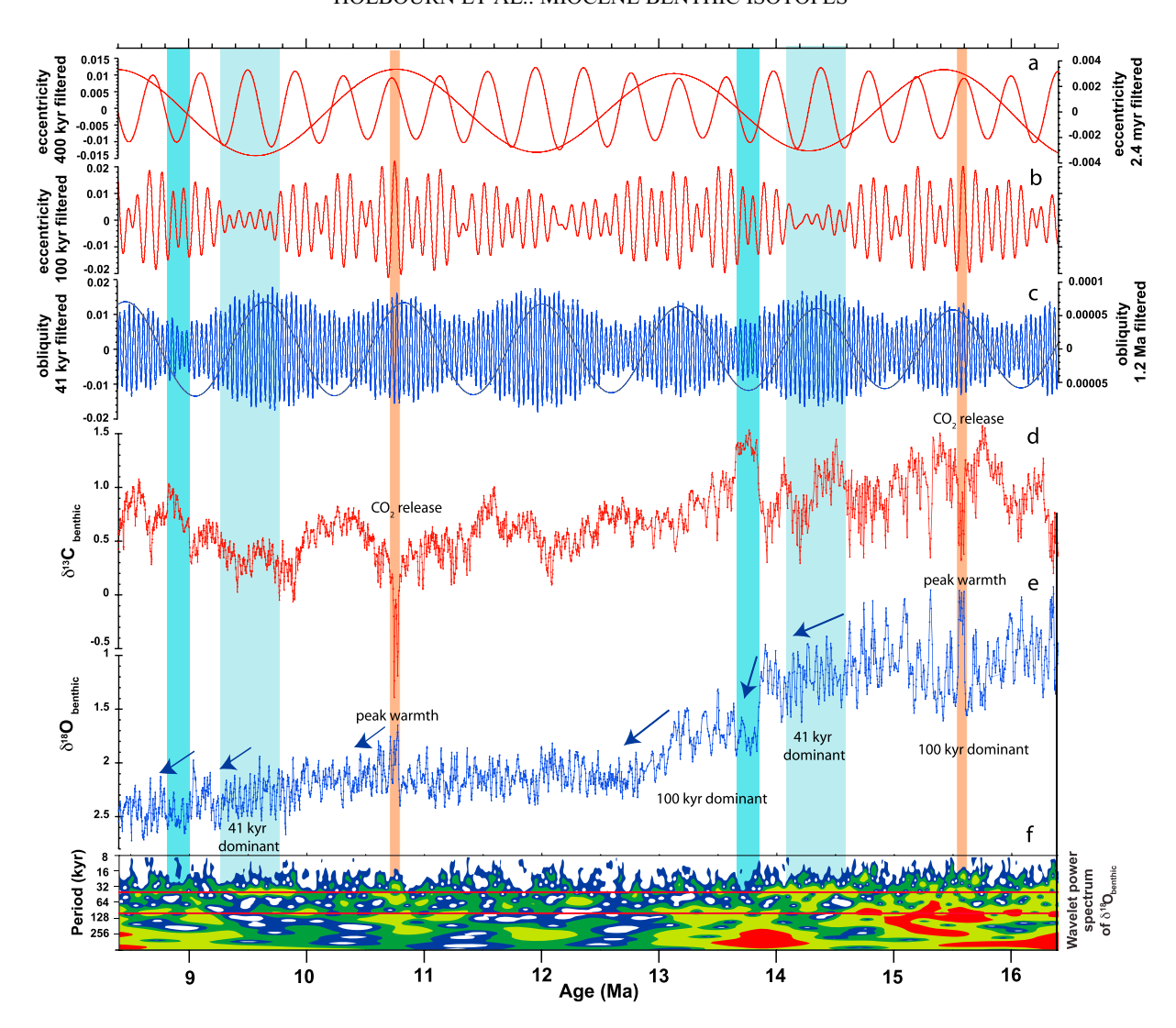


Figure 7. Comparison of benthic δ^{18} O and δ^{13} C data in ODP Site 1146 with orbital variability from Laskar et al. [2004] over 16.4–8.4 Ma interval. (a) 2.4 Myr filtered eccentricity (centered at frequency 0.0004166 with bandwidth 0.0001) and 400 kyr filtered eccentricity (centered at frequency 0.0025 with bandwidth 0.0005). (b) 100 kyr filtered eccentricity (centered at frequency 0.01 with bandwidth 0.004). (c) 1.2 Myr filtered obliquity (centered at frequency 0.00083 with bandwidth 0.0001) and 41 kyr filtered obliquity (centered at frequency 0.02433 with bandwidth 0.007). (d) Benthic δ^{13} C, 3 pt smoothed; (e) Benthic δ^{18} O, 3 pt smoothed, (f) Wavelet power spectrum of benthic δ^{18} O, settings as in Figure 4f. Orange bands mark transient warmings and negative δ^{13} C excursions at eccentricity maxima (100 and 400 kyr). Light blue shading highlights periods of low (100 kyr) eccentricity variability and high (41 kyr) obliquity variability, when δ^{18} O exhibits mainly 41 kyr variability. Darker blue bands mark cooling episodes concomitant with nodes in obliquity.

climate development, although the climatic response to astronomical forcing was essentially nonlinear.

[28] It was previously suggested that glaciations are typically enhanced during intervals of reduced amplitude variations in obliquity (obliquity nodes) coincident with low eccentricity [*Zachos et al.*, 2001b; *Pälike et al.*, 2006]. This confluence promotes high-latitude cooling, preventing ice from melting during summer, which is especially critical, when ice sheets are still highly dynamic [*DeConto et al.*, 2008]. Our extended data set shows that the major δ^{18} O excursion at ~13.9 Ma coincides with an obliquity node and that the somewhat smaller δ^{18} O step at ~9.0 Ma is associated with a similar orbital configuration (Figure 7). Interestingly, these

two events are both preceded by extended intervals of high-amplitude variations in obliquity, suggesting preconditioning of the climate system before extreme responses to 100 and 400 kyr eccentricity forcing during obliquity nodes. However, no positive δ^{18} O excursions coincide with obliquity nodes either during the warmer climate phase prior to 14.6 Ma or during the colder mode after 12.9 Ma, indicating that other triggering factors were also required to force the climate across critical thresholds. Studies of Pliocene-Pleistocene climate variations have shown, for instance, that changes in the ocean/atmosphere CO_2 exchange, latitudinal temperature gradient, meridional overturning circulation, and ice sheet hysteresis also exert major control on climate development through

intricate internal feedback processes [e.g., Fedorov et al., 2006; Denton et al., 2010; Sigman et al., 2010; Skinner et al., 2010].

[29] During warmer periods of Earth's history, the size and thickness of ice sheets probably play a crucial role, as a critical mass balance threshold needs to be reached in order to sustain ice growth. During the Miocene climatic optimum, when the latitudinal temperature gradient was relatively low and polar temperatures elevated, small ice sheets remained highly susceptible to summer radiative forcing. In contrast, prolonged periods of low summer insolation would inhibit melting and favor ice growth. However, as Antarctica became thermally more insulated following major ice sheet expansion and concomitant intensification of the Antarctic Circumpolar Current, moisture transfer from lower latitudes became reduced and further ice accumulation decreased. The marked decrease in $\delta^{18}O$ amplitude variability after ~12.9 Ma in Site 1146 suggests that a substantially drier, colder, and more stable climate became established over the Antarctic continent that likely reflected a long-term change from warm- to cold-based ice grounding after that time. Decreased sensitivity to eccentricity forcing and dampened δ^{18} O variability suggest that moisture transport became, as it is today [Jouzel et al., 2007], the dominant control on Antarctic ice sheet growth and that, after that time, fluctuations in surface mass budget became somewhat more comparable to Pleistocene variations.

5. Conclusion

[30] We constructed a high-resolution benthic stable isotope curve to evaluate long-term Miocene climate variability (16.4 to 8.4 Ma) and to investigate the pacing of high-latitude cooling during the transition from a warmer phase with reduced and highly dynamic Antarctic ice sheets to an increasingly glaciated mode with more permanent ice cover. Our extended record shows that the climatic optimum was characterized by high-amplitude climate variability with intense warming pulses associated with transient declines in deep water ventilation. The δ^{18} O succession indicates that highlatitude cooling and glaciation progressed in a series of incremental steps at ~14.6, 13.9, 13.1, 10.6, 9.9, and 9.0 Ma. Dampened δ^{18} O variability after 13 Ma indicates a more stable ice cover, leading us to speculate that latitudinal moisture transfer rather than radiative forcing became the dominant control of ice volume variations following Antarctic glacial expansion. Intense warming spikes at ~10.8-10.7 Ma suggest transient melting of polar ice and deep ocean warming during an unusual interval of remarkably high-amplitude variability in 100 kyr eccentricity. This long-term perspective demonstrates that astronomical forcing had a major impact on middle to late Miocene climate development. However, our study emphasizes the nonlinear response of the climate/ ocean system to astronomical forcing involving additional forcing factors with intricate feedback processes including CO₂ exchange between atmospheric and oceanic reservoirs, latitudinal temperature distribution, rates of meridional overturning circulation, and ice sheet hysteresis.

[31] **Acknowledgments.** This research used samples provided by the Ocean Drilling Program and was funded by the Deutsche Forschungsgemeinschaft (Grant KU649/30-1). We thank Heiko Pälike and two anonymous reviewers for helpful critical comments.

References

- Billups, K., and D. P. Schrag (2002), Paleotemperatures and ice-volume of the past 27 Myr revisited with paired Mg/Ca and ¹⁸O/¹⁶O measurements on benthic foraminifera, *Paleoceanography*, *17*(1), 1003, doi:10.1029/2000PA000567.
- Bohaty, S. M., J. C. Zachos, F. Florindo, and M. L. Delaney (2009), Coupled greenhouse warming and deep-sea acidification in the middle Eocene, *Paleoceanography*, 24, PA2207, doi:10.1029/2008PA001676.
- Cramer, B. S., J. R. Toggweiler, J. D. Wright, M. E. Katz, and K. G. Miller (2009), Ocean overturning since the Late Cretaceous: Inferences from a new benthic foraminiferal isotope compilation, *Paleoceanography*, 24, PA4216, doi:10.1029/2008PA001683.
- De Boer, B., R. S. W. Van de Wal, R. Bintanja, L. J. Lourens, and E. Tuenter (2010), Cenozoic global ice-volume and temperature simulations with 1-D ice-sheet models forced by benthic δ¹⁸O records, *Ann. Glaciol.*, *51*, 23–33.
- DeConto, R. M., D. Pollard, P. A. Wilson, H. Pälike, C. H. Lear, and M. Pagani (2008), Thresholds for Cenozoic bipolar glaciation, *Nature*, 455, 652–657.
- Denton, G. H., R. F. Anderson, J. R. Toggweiler, and R. L. Edwards (2010), The last termination, *Science*, *328*, 1652–1656, doi:10.1126/science.1184119.
- Dickens, G. R., J. R. O'Neil, D. K. Rea, and R. M. Owen (1995), Dissociation of oceanic methane hydrate as a cause of the carbon isotope excursion at the end of the Paleocene, *Paleoceanography*, 10, 965–971.
- Feakins, S. J., S. Warny, and J.-E. Lee (2012), Hydrologic cycling over Antarctica during the middle Miocene warming, *Nat. Geosci.*, 5, 557–560, doi:10.1038/ngeo1498.
- Fedorov, A. V., P. S. Dekens, M. McCarthy, A. C. Ravelo, P. B. de Menocal, M. Barreiro, R. C. Pacanowski, and S. G. Philander (2006), The Pliocene paradox (mechanisms for a permanent El Niño), *Science*, 312, 1485, doi:10.1126/science.1122666.
- Flower, B. P., and J. P. Kennett (1993), Middle Miocene ocean-climate transition: High resolution oxygen and carbon isotopic records from DSDP Site 588A, southwest Pacific, *Paleoceanography*, 8, 811–843.
- Flower, B. P., and J. P. Kennett (1995), Middle Miocene deep water paleoceanography in the southwest Pacific: Relations with East Antarctic ice sheet development, *Paleoceanography*, 10, 1095–1112.
- Gradstein, F. M., et al. (2012), *The Geologic Time Scale 2012: Boston*, Elsevier, USA, doi:10.1016/B978-0-444-59425-9.00004-4.
- Hauptvogel, D. W., and S. Passchier (2012), Early–Middle Miocene (17–14 Ma) Antarctic ice dynamics reconstructed from the heavy mineral provenance in the AND-2A drill core Ross Sea, Antarctica, *Global Planet. Change*, 82–83, 38–50, doi:10.1016/j.gloplacha.2011.11.003.
- Haywood, A. M., et al. (2009), Middle Miocene to Pliocene history of Antarctica and the Southern Ocean, in *Developments in Earth and Environmental Sciences*, vol. 8, edited by F. Florindo and M. Siegert, pp. 401–463, Elsevier, Antarctic Climate Evolution, ISBN:978-0-444-52847-6.
- Holbourn, A. E., W. Kuhnt, M. Schulz, and H. Erlenkeuser (2005), Impacts of orbital forcing and atmospheric CO₂ on Miocene ice-sheet expansion, *Nature*, 438, 483–487, doi:10.1038/nature04123.
- Holbourn, A. E., W. Kuhnt, M. Schulz, J.-A. Flores, and N. Andersen (2007), Orbitally-paced climate evolution during the middle Miocene "Monterey" carbon-isotope excursion, *Earth Planet. Sci. Lett.*, 261, 534–550.
- Huang, C.-Y., W.-Y. Wu, C.-P. Chang, S. Tsao, P. B. Yuan, C.-W. Lin, and X. Kuan-Yuan (1997), Tectonic evolution of accretionary prism in the arccontinent collision terrane of Taiwan, *Tectonophysics*, 281, 31–51.
- Imbrie, J., and J. Z. Imbrie (1980), Modeling the climatic response to orbital variations, *Sci. New Series*, 207(4434), 943–953.
- John, C. M., G. D. Karner, E. Browning, R. M. Leckie, Z. Mateo, B. Carson, and C. Lowery (2001), Timing and magnitude of Miocene eustasy derived from the mixed siliciclastic-carbonate stratigraphic record of the northeastern Australian margin, *Earth Planet. Sci. Lett.*, 304, 455–467.
- Jouzel, J., et al. (2007), Orbital and millennial Antarctic climate variability over the past 800,000 years, Science, 317, 793, doi:10.1126/science.1141038.
- Kominz, M. A., J. V. Browning, K. G. Miller, P. J. Sugarman, S. Mizintsevaw, and C. R. Scotese (2008), Late Cretaceous to Miocene sea-level estimates from the New Jersey and Delaware coastal plain core holes: An error analysis, *Basin Res.*, 20, 211–226, doi:10.1111/j.1365-2117.2008.00354.x.
- Laskar, J., P. Robutel, F. Joutel, M. Gastineau, A. Correia, and B. A. Levrard (2004), Long term numerical solution for the insolation quantities of the Earth, *Astron. Astrophys.*, 428, 261–285.
- Lear, C. H., E. M. Mawbey, and Y. Rosenthal (2010), Cenozoic benthic foraminiferal Mg/Ca and Li/Ca records: Toward unlocking temperatures and saturation states, *Paleoceanography*, 25, PA4215, doi:10.1029/ 2009PA001880.
- Lewis, A. R., D. R. Marchant, D. E. Kowalewski, S. L. Baldwin, and L. E. Webb (2006), The age and origin of the Labyrinth, western Dry Valleys Antarctica: Evidence for extensive middle Miocene subglacial floods and freshwater discharge to the Southern Ocean, *Geology*, 34, 513–516, doi:10.1130/G22145.1.

- Lewis, A. R., D. R. Marchant, A. C. Ashworth, S. R. Hemming, and M. L. Machlus (2007), Major middle Miocene global climate change: Evidence from East Antarctica and the Transantarctic Mountains, *GSA Bull.*, *119*, 1449–1461, doi:10.1130/0016-7606(2007)119[1449: MMMGCC]2.0.CO;2.
- Lewis, A. R., et al. (2008), Mid-Miocene cooling and the extinction of tundra in continental Antarctica, *Proc. Natl. Acad. Sci. U.S.A.*, 105, 10,676–10,680, doi:10.1073/pnas.0802501105.
- Lhomme, N., G. K. C. Clarke, and C. Ritz (2005), Global budget of water isotopes inferred from polar ice sheets, *Geophys. Res. Lett.*, 32, L20502, doi:10.1029/2005GL023774.
- Lisiecki, L. E., and M. E. Raymo (2005), A Pliocene-Pleistocene stack of 57 globally distributed benthic d¹⁸O records, *Paleoceanography*, 20, PA1003, doi:10.1029/2004PA001071.
- Lourens, L. J., A. Sluijs, D. Kroon, J. C. Zachos, E. Tomas, U. Röhl, J. Bowles, and I. Raffi (2005), Astronomical pacing of late Paleocene to early Eocene global warming events, *Nature*, 435, 1083–1087, doi:10.1038/nature03814
- Lyle, M., J. Barron, T. J. Bralower, M. Huber, A. Olivarez Lyle, A. C. Ravelo, D. K. Rea, and P. A. Wilson (2008), Pacific Ocean and Cenozoic evolution of climate, *Rev. Geophys.*, 46, RG2002, doi:10.1029/2005RG000190.
- Miller, K. G., J. D. Wright, and R. G. Fairbanks (1991), Unlocking the ice house: Oligocene-Miocene oxygen isotopes, eustacy and margin erosion, *J. Geophys. Res.*, *96*, 6829–6848.
- Muller, R. A., and J. MacDonald (2000), *Ice Ages and Astronomical Causes, Data, Spectral Analysis and Mechanisms*, pp. 318, Springer Praxis Books in Environmental Sciences, Springer in association with Praxis Publishing, Chichester, UK.
- Nathan, S. A., and R. M. Leckie (2003), Miocene planktonic foraminiferal biostratigraphy of Sites 1143 and 1146, ODP Leg 184, South China Sea, in *Scientific Results of the Ocean Drilling Program*, edited by W. L. Prell et al., 184, College Station, TX, [Online]. Available from World Wide Web: http://www-odp.tamu.edu/publications/184 SR/219/219.htm.
- Paillard, D., L. Labeyrie, and P. Yiou (1996), Macintosh program performs time-series analysis, EOS Trans. AGU, 77, 379.
- Pälike, H., J. Frazier, and J. C. Zachos (2006), Extended orbitally forced paleoclimatic records from the equatorial Atlantic Ceara Rise, *Quat. Sci. Rev.*, 25, 3138–3149, doi:10.1016/j.quascirev.2006.02.011.
- Poore, H. R., R. Samworth, N. J. White, S. M. Jones, and I. N. McCave (2006), Neogene overflow of Northern Component Water at the Greenland-Scotland Ridge, *Geochem. Geophys. Geosyst.*, 7, Q06010, doi:10.1029/2005GC001085.
- Raffi, I., J. Backman, E. Fornaciari, H. Pälike, D. Rio, L. Lourens, and F. Hilgen (2006), A review of calcareous nannofossil astrobiochronology encompassing the past 25 million years, *Quat. Sci. Rev.*, 25, 3113–3137.
- Sexton, P. F., R. D. Norris, P. A. Wilson, H. Pälike, T. Westerhold, U. Röhl, C. T. Bolton, and S. Gibbs (2011), Eocene global warming events driven

- by ventilation of oceanic dissolved organic carbon, *Nature*, 471, 349–353, doi:10.1038/nature09826.
- Shackleton, N. J. (2001), Milankovitch in the Miocene, Eos Transactions AGU, 82(47) Fall Meeting Supplement, Abstract U11A-12.
- Sigman, D. M., M. P. Hain, and G. H. Haug (2010), The polar ocean and glacial cycles in atmospheric CO₂ concentration, *Nature*, 466, doi:10.1038/nature09149.
- Skinner, L. C., S. Fallon, C. Waelbroeck, E. Michel, and S. Barker (2010), Ventilation of the deep Southern Ocean and deglacial CO2 rise, *Science*, 328, 1147–1151, doi:10.1126/science.1183627.
- Skinner, L. C., A. E. Scrivner, D. Vance, S. Barker, S. Fallon, and C. Waelbroeck (2013), North Atlantic versus Southern Ocean contributions to a deglacial surge in deep ocean ventilation, *Geology*, 41, 667–670, doi:10.1130/G34133.1.
- Stöckli, R., E. Vermote, N. Saleous, R. Simmon, and D. Herring (2005), The Blue Marble Next Generation—A true color earth dataset including seasonal dynamics from MODIS. Published by the NASA Earth Observatory. Corresponding author: rstockli@climate.gsfc.nasa.gov.
- Torrence, C., and G. P. Compo (1998), A practical guide to wavelet analysis, *Bull. Am. Meteorol. Soc.*, 79, 61–78.
- Wade, B. S., P. N. Pearson, W. A. Berggren, and H. Pälike (2011), Review and revision of Cenozoic tropical planktonic foraminiferal biostratigraphy and calibration to the geomagnetic polarity and astronomical time scale, *Earth Sci. Rev.*, 104, 111–142.
- Wang, P., et al. (2000), Proceedings of the Ocean Drilling Program, Initial Reports 184 [CD-ROM]. Available from: Ocean Drilling Program, Texas A&M University, College Station TX 77845–9547, USA.
- Warny, S., A. R. Askin, M. J. Hannah, B. A. R. Mohr, J. I. Raine, D. N. Harwood, F. Florindo, and the SMS Science Team (2009), Palynomorphs from a sediment core reveal a sudden remarkably warm Antarctica during the middle Miocene, *Geology*, *37*, 955–958, doi:10.1130/G30139A.1.
- Westerhold, T., T. Bickert, and U. Röhl (2005), Middle to late Miocene oxygen isotope stratigraphy of ODP site 1085 (SE Atlantic): New constrains on Miocene climate variability and sea-level fluctuations, *Palaeogeogr. Palaeoclimatol. Palaeoecol.*, 217, 205–222.
- Woodruff, F., and S. Savin (1991), Mid-Miocene isotope stratigraphy in the deep sea: High resolution correlations, paleoclimatic cycles, and sediment preservation, *Paleoceanography*, 6, 755–806.Zachos, J., M. Pagani, L. Sloan, E. Thomas, and K. Billups (2001a), Trends,
- Zachos, J., M. Pagani, L. Sloan, E. Thomas, and K. Billups (2001a), Trends, rhythms, and aberrations in global climate 65 Ma to present, *Science*, 292, 686–693.
- Zachos, J., N. J. Shackleton, J. S. Revenaugh, H. Pälike, and B. P. Flower (2001b), Climate response to orbital forcing across the Oligocene-Miocene boundary, *Science*, 292, 274–278.
- Zachos, J. C., G. R. Dickens, and R. E. Zeebe (2008), An early Cenozoic perspective on greenhouse warming and carbon-cycle dynamics, *Nature*, 451, 279–283, doi:10.1038/nature06588.